


# New method for fitting complex resonance curve to study nonlinear superconducting resonators

X Dai<sup>1</sup>, X Liu<sup>2,\*</sup>, Q He<sup>3</sup>, Y Chen<sup>1</sup>, Z Mai<sup>1</sup>, Z Shi<sup>1</sup>, W Guo<sup>1</sup>, Y Wang<sup>1,\*</sup> , L F Wei<sup>3</sup>, M R Vissers<sup>4</sup> and J Gao<sup>4</sup>

<sup>1</sup> Quantum Optoelectronics Laboratory, School of Physical Science and Technology, Southwest Jiaotong University, Chengdu 610031, People's Republic of China

<sup>2</sup> National Institute of Metrology, Beijing 100029, People's Republic of China

<sup>3</sup> Information Quantum Technology Laboratory, School of Information Science and Technology, Southwest Jiaotong University, Chengdu 610031, People's Republic of China

<sup>4</sup> National Institute of Standards and Technology, Boulder, CO 80305, United States of America

E-mail: [qubit@swjtu.edu.cn](mailto:qubit@swjtu.edu.cn) and [liuxl@nim.ac.cn](mailto:liuxl@nim.ac.cn)

Received 2 June 2022, revised 12 November 2022

Accepted for publication 21 November 2022

Published 29 November 2022



## Abstract

We present a new fitting method that can robustly and accurately fit the complex transmission curve of a superconducting resonator in the nonlinear regime. This method takes into account the varying internal current in the resonator at different frequencies and the nonlinear dependence of the inductance on the internal current  $L = L_0(1 + I^2/I_*^2)$ , where  $I_*$  is a characteristic current. We demonstrate using this method to retrieve important resonator parameters, such as the quality factor and the resonance frequency, from resonators driven below, near, and above bifurcation. We further use this method to retrieve  $I_*$  for lumped-element TiN resonators with various inductor designs. By fitting the resonance frequency shift at different readout powers of each resonator, we can determine the characteristic current  $I_*$ , which is found to be linearly related to the cross-sectional area of the narrow inductor strip. Our method has wide applications in superconducting detector, superconducting qubit and parametric amplifier data analysis where the resonator is driven in the nonlinear regime.

Keywords: nonlinear superconducting resonator, kinetic inductance detector, superconducting microresonator

(Some figures may appear in colour only in the online journal)

## 1. Introduction

Superconducting microresonators [1] have been widely used in many scientific applications, such as photon detection [2], superconducting quantum computing [3], and quantum-limited parametric amplifiers [4]. For example, microwave kinetic inductance detectors (MKIDs) [5] are

high-quality (high- $Q$ ) superconducting microresonators multiplexed in the microwave frequency range into large arrays for sensitive power detection at millimeter and sub-millimeter wavelengths [6–8]. MKIDs can also serve as single photon-counting and energy-resolving detectors for x-ray/ultraviolet/optical/near-infrared photons [9–14].

It is well known that the behavior of the superconducting microresonator is readout power dependent. In particular, the resonance curve becomes distorted as the readout power increases. Above a certain power level known as the

\* Authors to whom any correspondence should be addressed.

bifurcation point [1] the resonance curve becomes discontinuous and standard fitting models no longer apply. While various physical mechanisms [15] may lead to nonlinearity in the resonator, including power-dependent current distribution [16], effective quasi-particle temperature variations due to readout power [17, 18], local heating of weak links [19], the intrinsic kinetic inductance nonlinearity [20] usually dominate for high- $Q$  resonators at temperatures well below the transition temperature  $T_c$ . MKIDs usually operate at a high readout power close to bifurcation to maximize the signal-to-noise ratio. Operation of MKIDs beyond the onset of bifurcation has been studied by [21]. Besides, the nonlinearity in the Josephson junction inductance and the kinetic inductance are utilized to construct quantum-limited parametric amplifiers, including Josephson parametric amplifier (JPA) [22], Josephson junction travelling-wave parametric amplifier (JJ-TWPA) [23] and kinetic-inductance traveling-wave parametric amplifier (KI-TWPA) [24–26], as well as to create novel tunable superconducting devices, such as frequency and coupling tunable superconducting resonator devices [27, 28]. All of these devices would be better understood by analyzing resonator behavior in the nonlinear regime.

In this paper, we develop a new fitting method and apply it to study the nonlinear superconducting microresonators. First, we present a new and robust fitting model to accurately extract useful resonator parameters in the nonlinear regime. Our method fits in the complex transmission  $S_{21}$  plane and is different from the approach used in [21] where an implicit cubic equation is solved. Second, we apply our fitting method to a superconducting TiN resonator made from TiN/Ti/TiN trilayer films [6] and demonstrate that our method can fit the transmission data below, near and above the bifurcation point. Third, we explore the nonlinearity and derive the characteristic current  $I_*$  for lumped-element TiN resonators with various inductor geometries. The effects of non-ideal lumped circuits are also considered. As expected, the derived  $I_*$  is proportional to the width (cross-sectional area since the thickness is fixed) of the narrow inductor strip, validating our nonlinear fitting method. This allows us to reliably predict the maximum readout power once the resonator geometry and material are chosen.

## 2. Fitting principle

### 2.1. Linear fitting principle

The complex transmission at low power for a superconducting resonator coupled to a feed-line is given by [29, 30]:

$$z(f) = S_{21}(f) = Ae^{-2\pi jf\tau} \left[ 1 - \frac{Q/Q_c e^{j\phi_0}}{1 + 2jQ \left( \frac{f-f_{r0}}{f_{r0}} \right)} \right], \quad (1)$$

where  $f$  is the probe frequency,  $A$  is a complex constant accounting for the gain, loss and phase shift through the system,  $\tau$  is the cable delay constant depending on the length of

cables,  $\phi_0$  accounts for impedance mismatch, and  $j$  is the imaginary unit. The important resonance parameters include the total quality factor  $Q$ , coupling quality factor  $Q_c$  and resonance frequency  $f_{r0}$ . In the linear regime (low readout power), many approaches have been developed in order to precisely determine the resonance parameters [31]. In the following, we first briefly review our linear fitting principle, which has been well discussed in appendix E in Gao's thesis [32].

As shown in figure 1(a), the measured raw data (a set of  $\{f_i, z_i\}$ , with  $i = 1, 2, \dots$ , denoting the  $i$ th data point) for a superconducting TiN resonator driven at low power is plotted as green dots. After removing the cable delay term by multiplying  $z_i$  with  $e^{2\pi j(f_i - f_i)\tau}$ , we obtain the orange trace, which can be fitted by a black circle centered at  $z_c$  (black cross) using a circle fitting procedure [33]. Then the phase angle  $\theta$  of each data point with respect to  $z_c$  as a function of  $f$  is fitted to the model:

$$\theta(f_i) = \theta_0 + 2\tan^{-1} [-2Q(f_i - f_{r0})/f_{r0}], \quad (2)$$

where  $\theta_0$  is the phase angle at resonance frequency. By implementing a robust nonlinear least-squares minimization:

$$\min \left\{ \sum_{i=1}^n |\theta_i - \theta(f_i)|^2 \right\}, \quad (3)$$

where  $\theta_i$  is the measured phase angle at  $f_i$ , we can determine the fitting parameters including  $f_{r0}$ ,  $Q$  and  $\theta_0$ . The red curve in figure 1(b) is the fitted phase-frequency curve, which shows good agreement with the experimental data (blue curve). The coupling quality factor  $Q_c$  and internal quality factor  $Q_i$  can then be extracted from a geometric relationship determined by equation (1), which has been discussed in [29].

### 2.2. Nonlinear fitting principle

As the readout power increases, the measured resonance curve becomes distorted. At a certain power level (bifurcation point), the discontinuity begins to appear in the transmission curve. This phenomenon can be qualitatively understood by considering the internal current in the resonator and its induced frequency shift through the nonlinear kinetic inductance. As the frequency sweeps upward towards the resonance frequency, the internal current increases, leading to an increase in the kinetic inductance, which in turn causes the resonance frequency to shift downward. This positive feedback further reduces the frequency detuning, which can result in the switching behavior seen in transmission.

Here we introduce a nonlinear fitting method, which can be seen as an extension from the above linear fitting method. The key modification is that we introduce a current-dependent instantaneous resonance frequency  $f_r(I)$  to replace the fixed  $f_{r0}$  in equation (1):

$$z(f) = Ae^{-2\pi jf\tau} \left[ 1 - \frac{Q/Q_c e^{j\phi_0}}{1 + 2jQ \left( \frac{f-f_r(I)}{f_r(I)} \right)} \right], \quad (4)$$

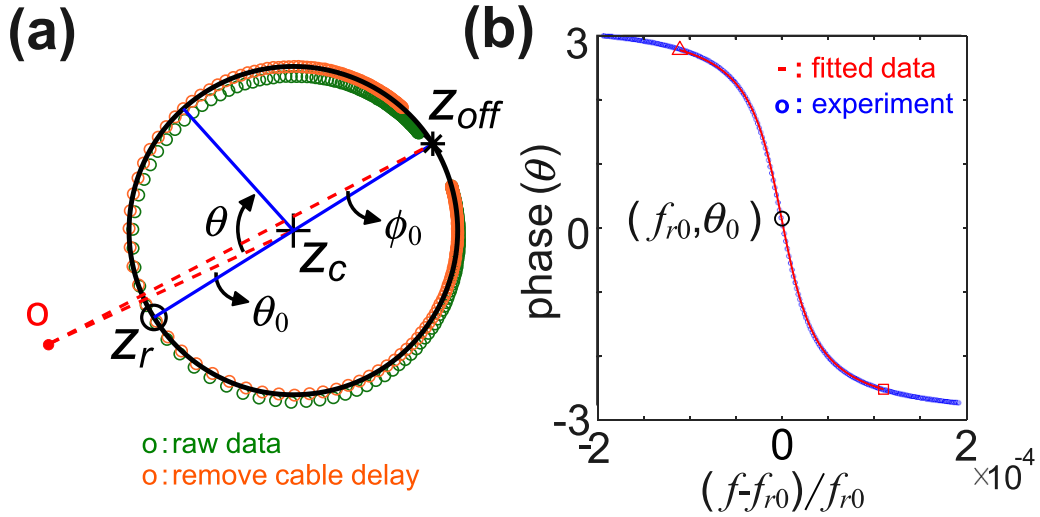


**Figure 1.** (a) The linear fitting principle in the complex plane at low readout power.  $O$  is the origin,  $z_c$  is the resonance circle center, and  $\theta$  is the measured phase angle with respect to  $z_c$  at the probe frequency  $f$ . By fitting  $\theta$  at each data point with  $f$  to equation (2), we can obtain the resonance point  $z_r$  and the off-resonance point  $z_{\text{off}}$ . Note that  $z_r$ ,  $z_c$  and  $z_{\text{off}}$  are collinear points. The geometric relationship between  $\theta_0$  and  $\phi_0$  is also shown in this figure. (b) Experimental and fitted phase-frequency curve. We fit the data in a frequency span  $\approx 4f_{r0}/Q$ , between the symbols  $\triangle$  and  $\square$ . The black circle marks the resonance point with phase angle  $\theta_0$ .

where  $I$  is the magnitude of the internal current in the resonator. Note that we assume the other parameters ( $Q$ ,  $Q_c$ , etc) are current independent, which is valid for pure nonlinear inductive effect with very low dissipation. Considering the quadratic current-dependent nonlinearity in the kinetic inductance [34, 35]:

$$L_k(I) = L_{k0} \left[ 1 + \left( \frac{I}{I_*} \right)^2 \right], \quad (5)$$

where  $L_{k0}$  is the kinetic inductance in the zero current limit and  $I_*$  is a characteristic current on the order of the critical current, the instantaneous resonance frequency shift can be written as:

$$f_r(I) = f_{r0} \left( 1 - \frac{\alpha I^2}{2I_*^2} \right), \quad (6)$$

where  $f_{r0} = f_r(I = 0)$  can be obtained by a linear fit applied to the low-power  $S_{21}$  data and  $\alpha$  is the kinetic inductance fraction.

Next, we derive an important relationship in the complex  $z$ -plane that allows us to embed equation (6) into the fitting model. Figure 2(a) shows a 3-port network model of a lumped-element resonator and figure 2(b) is a plot of the complex  $S_{21}$  interpreted as a phasor diagram of the output waves. The output waves from port-2 consist of two components: the directly transmitted wave  $A_2$  and the wave leaked out of the resonator to port-2  $B_2$ .  $A_2$  can be understood as the background transmission without any resonator or far from the resonance, thus it is indicated by the blue arrow from origin to off-resonance point ( $z_{\text{off}}$ ) in figure 2(b). On the other hand,  $B_2$  is indicated by the red arrow from  $z_{\text{off}}$  to a certain probe frequency point ( $z$ -point). The sum of  $A_2$  and  $B_2$  results in the forward transmission  $S_{21}$  at point  $z$ . Because the leakage wave  $|B_2|^2 \propto E|S_{31}|^2$ ,

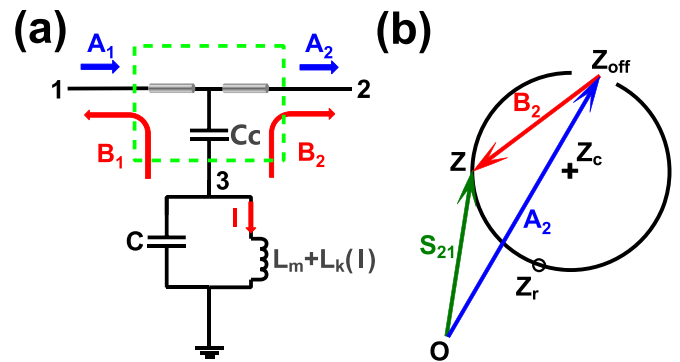


**Figure 2.** (a) 3-port network model for a lumped-element resonator, which is capacitively coupled to the feed-line. The resonator has a magnetic inductance  $L_m$  and a current-dependent kinetic inductance  $L_k(I)$ .  $A_1$  is the incident wave into port-1 and  $A_2$  is the directly transmitted wave to port-2. Around resonance, there are reflected waves from the resonator (port-3) to port-1 and port-2, which are denoted by  $B_1$  and  $B_2$  respectively. (b) The complex  $S_{21}$  is interpreted as a phasor diagram of the output waves at port-2. We prove that the resonator current at a probe frequency ( $z$ -point) is proportional to  $|B_2|$ , i.e. the magnitude of the difference in the complex  $S_{21}$  between the probe frequency and the off-resonance point  $z_{\text{off}}$ .

where  $E = LI^2/2$  is the energy stored in the resonator and the scattering parameter  $S_{31}$  is unchanged in a narrow frequency band, we arrive at the relationship:

$$|B_2|^2 = |z - z_{\text{off}}|^2 \propto I^2. \quad (7)$$

Equation (7) shows that the current in the resonator is proportional to the magnitude of the complex  $S_{21}$  value's difference between the probe frequency and the off-resonance point. With equation (7), we can rewrite equation (6) into:

$$f_r(I) = f_{r0} \left( 1 - \beta |z - z_{\text{off}}|^2 \right), \quad (8)$$

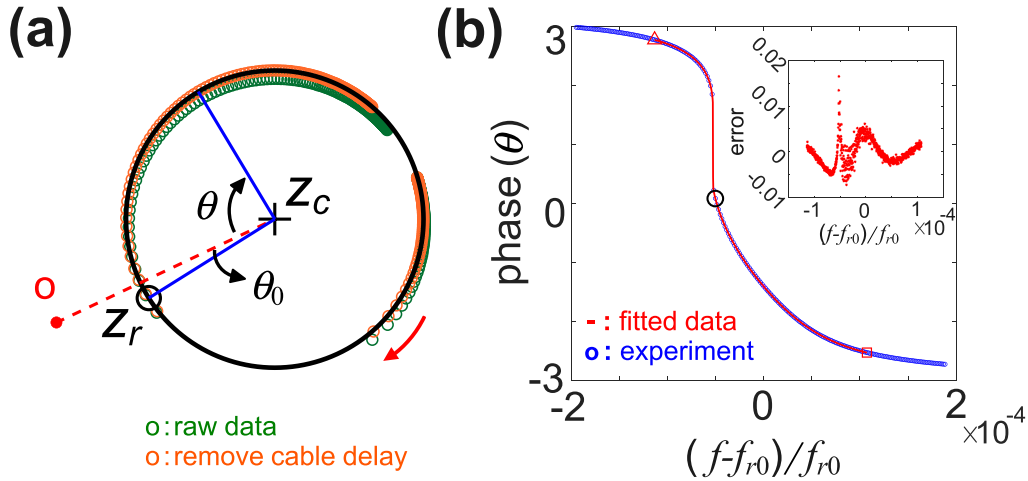


**Figure 3.** (a) Nonlinear fit of the resonance circle around the bifurcation point in the complex plane. The red arrow shows the direction of increasing frequency. The data points are crowded on the high frequency side and sparse on the low frequency side around the discontinuity. (b) Experimental and fitted phase-frequency curve, showing good agreements. The resonance frequency is shifted to a lower value below  $f_{r0}$ . The inset shows the small fitted phase error (difference between the measured and fitted phase) with frequency.

where  $\beta$  is a proportional factor. Finally, the phase-frequency fitting model equation (2) is modified to:

$$\theta(f_i) = \theta_0 + 2 \tan^{-1} \left[ -2Q(f_i - f_{r0} + \beta |z(f_i) - z_{\text{off}}|^2) / f_{r0} \right]. \quad (9)$$

In practice,  $f_{r0}$ ,  $Q$ ,  $\beta$ ,  $\theta_0$  and  $z_{\text{off}}$  can all be determined through this nonlinear fitting procedure.

Figure 3 shows the nonlinear fitting results around the bifurcation point. Compared to figure 1, the same resonator is driven at a microwave power of 8 dB higher. We can see a discontinuity in the complex transmission (figure 3(a)) and phase-frequency curve (figure 3(b)), which both fit well with our method. The inset in figure 3(b) is a plot of the fitted phase error as a function of frequency, showing that the typical phase error is within 0.01 radian. Here we want to emphasize that these data can also be fitted well by using the method in [21]. However, the authors in [21] have to solve an implicit cubic equation with a trial nonlinear parameter (see equation (10)) to obtain the current-dependent resonance frequency  $f_r(I)$ , which complicates their fitting procedure. Our approach can explicitly express  $f_r(I)$  with equation (8) and embed it into the fitting model (equation (9)), so that a robust nonlinear least-squares minimization can be directly applied to the phase-frequency data. Therefore our nonlinear fitting method is easier and more efficient to implement. Furthermore, our method can be easily extended to study nonlinear kinetic inductance with higher-order current dependence, e.g. the case when  $I^4$  terms need to be taken into account for higher powers.

### 3. Application to TiN resonators

Our resonator devices are fabricated from a thin ( $\approx 18$  nm thick) superconducting TiN/Ti/TiN trilayer film ( $T_c \approx 1.4$  K) on 380  $\mu\text{m}$  thick Si substrate. The photon-noise limited

sensitivity has been experimentally demonstrated at 250  $\mu\text{m}$  in the feedhorn-coupled MKIDs made of the TiN trilayer film [6]. Figure 4(a) shows a standard lumped-element resonator (referred to ‘standard resonator’ in the following) design comprising a large interdigitated capacitor (IDC) in parallel with a narrow one-turn inductive strip (inductor). By comparing the resonance frequency from simulation and experiment, we obtain the sheet inductance of the TiN trilayer film  $\approx 71.1$  pH/ $\square$ . From the simulations, we also obtain the IDC capacitance  $C \approx 2.90$  pF. This allows us to determine the total inductance of the standard resonator  $L_0 \approx 7.77$  nH due to the measured resonance frequency  $\approx 1.06$  GHz. Figure 4(b) shows the simulated current density distribution on resonance, where we can see the current is uniformly distributed in the narrow inductor strip.

To experimentally study the kinetic inductance nonlinearity, we fabricate two types of chips (labeled as Chip1 and Chip2) and each chip has a group of resonators with same IDC but different inductor designs. Both Chip1 and Chip2 include a standard resonator. For Chip1, we change  $l_{\text{ind}}$  and  $w_{\text{ind}}$  while roughly fixing the value of  $l_{\text{ind}}/w_{\text{ind}}$  so that all resonators have approximately the same inductance and therefore similar resonance frequencies. For Chip2, we study resonators with combinational designs of different  $l_{\text{ind}}$  and  $w_{\text{ind}}$ . The detailed designs of resonators on Chip1 and Chip2 are listed in appendix C (see tables C1 and C2).

The tested chip is glued into a copper box, which is placed at the cold stage in an adiabatic demagnetization refrigerator (ADR) with a base temperature of 40 mK. The input excitation signal is generated by a microwave source and attenuated by about 40 dB before entering the chip box. The output signal is amplified by a low-noise SiGe amplifier at 3 K stage and further amplified by a room-temperature microwave amplifier. The complex transmission  $S_{21}$  is then measured with a vector network analyzer (VNA).

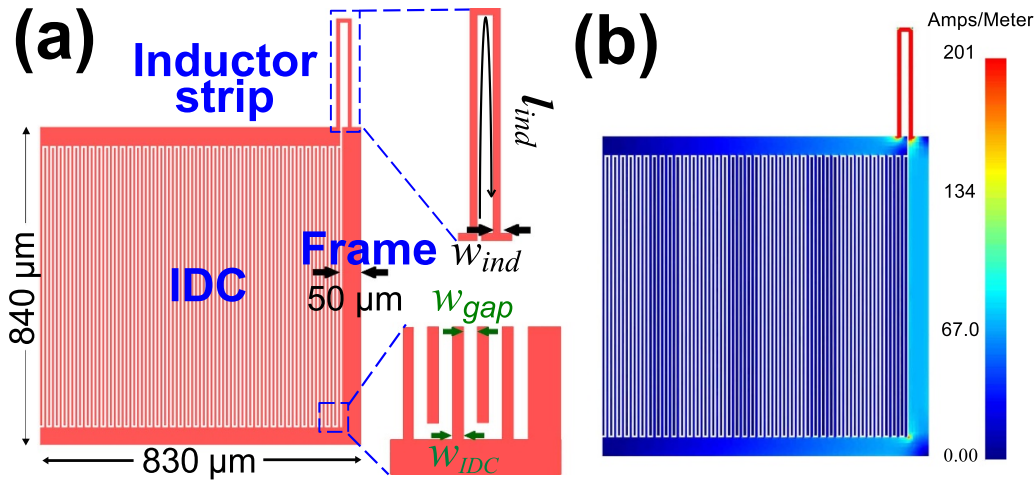


**Figure 4.** (a) Standard design of TiN trilayer lumped-element resonator: inductor length  $l_{ind} = 590 \mu\text{m}$ , inductor width  $w_{ind} = 10 \mu\text{m}$ , IDC finger width  $w_{IDC} = 5 \mu\text{m}$ , IDC finger gap  $w_{gap} = 5 \mu\text{m}$ , IDC frame width =  $50 \mu\text{m}$  and IDC area  $\approx 0.8 \text{ mm} \times 0.8 \text{ mm}$ . (b) Simulation shows the current is mainly distributed in the narrow inductor strip and the current in the IDC fingers is considerably smaller. Because the resonator is not an ideal lumped-element circuit, there is a finite current distribution in the IDC frame (upper, lower and right side of IDC) which has a finite contribution to the total inductance of the resonator.

Figure 5(a) shows the measured  $|S_{21}|^2$  with upward frequency sweeping for the standard resonator (on Chip1) at four different readout powers. A parameter  $a$ , which is proportional to the readout power, can be introduced to characterize the nonlinearity [21]:

$$a = \frac{\alpha \omega_r C P_{in} Q^3}{Q_c I_*^2}, \quad (10)$$

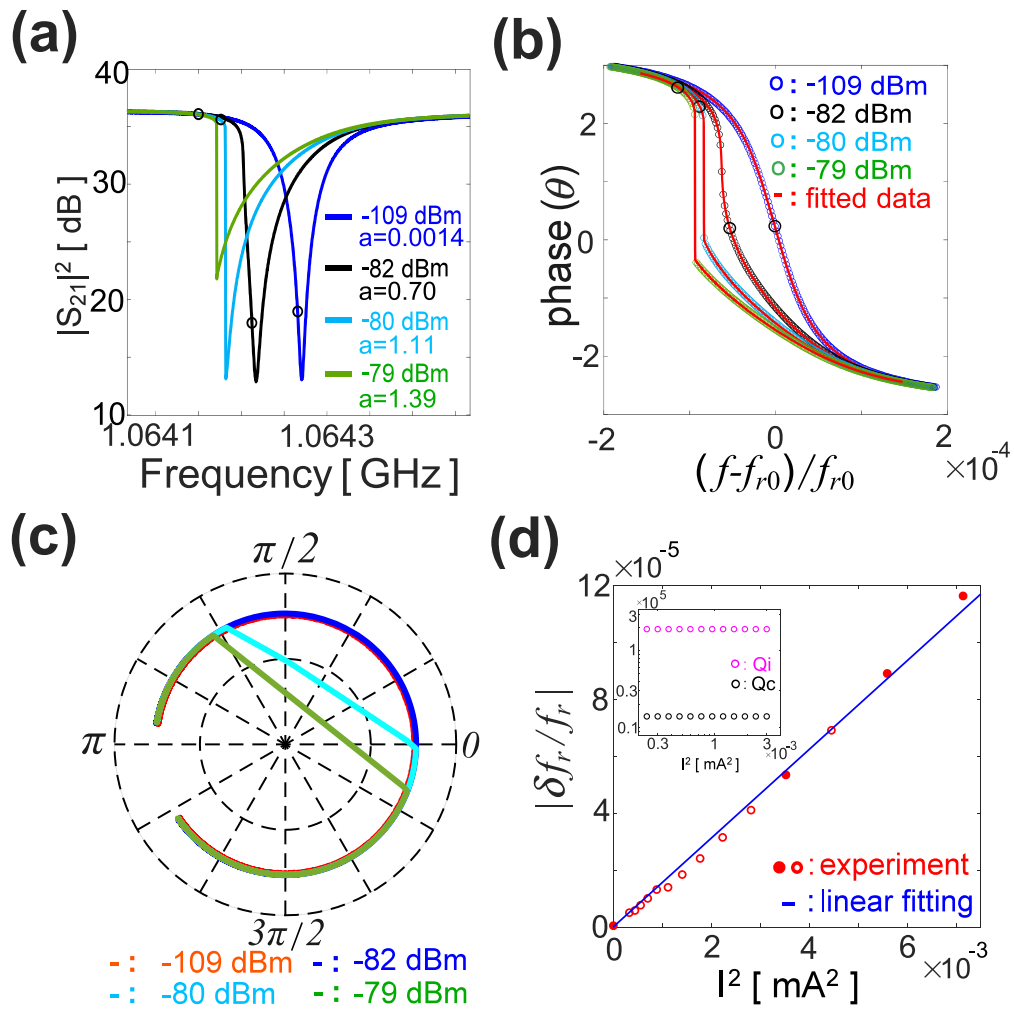
where  $P_{in}$  is the input power to the feed-line,  $C$  is the resonator capacitance and  $\omega_r = 2\pi f_r$  is the resonance frequency. To calculate  $a$ , we need to know all the parameters in equation (10). Among these parameters,  $Q$  and  $Q_c$  can be obtained from fitting, while the determination of  $P_{in}$ ,  $\alpha$  and  $I_*$  will be discussed in next paragraph. For figure 5(a),  $a$  ranges from 0.0014 to 1.39, corresponding to the conditions from far below to well above bifurcation because  $a \approx 0.8$  corresponds to the onset of bifurcation [21]. With increasing power, the resonance shifts to lower frequency and a sharp edge develops on the left side of the resonance dip. Figure 5(b) shows the measured and fitted phase-frequency curves. With increasing power, the data points become sparse around resonance and finally a discontinuity shows up. The good agreements between experiments and fittings demonstrate that our method can faithfully fit data below, near and above bifurcation. Figure 5(c) shows the measured transmission in the complex plane. All resonance circles have the same radius, indicating the purely reactive effects are dominant.

Figure 5(d) shows the measured fractional resonance frequency shift  $\delta f_r/f_0$  as a function of the square of resonator current  $I^2$ , demonstrating a linear relationship between  $\delta f_r/f_0$  and  $I^2$ . On resonance and for perfect impedance matching conditions, the resonance current can be obtained from the following expression (see appendix A):

$$I^2 = \frac{2\omega_r C P_{in} Q^2}{Q_c}. \quad (11)$$

In principle,  $P_{in}$  can be calculated by subtracting the circuit attenuation and losses before the feed-line from the nominal readout power. However, it is difficult to exactly determine  $P_{in}$  due to difficulties in measuring cryogenic attenuation and losses, which are both temperature and frequency dependent. Also because equation (11) is not valid for impedance mismatching conditions, the absolute value of  $I^2$  can only be determined within a few dB accuracy. From the slope of figure 5(d) and using equation (6), one can derive the characteristic current  $I_*$  once the kinetic inductance fraction  $\alpha$  is known. If we take the resonator as an ideal lumped-element circuit, i.e. the current-induced kinetic inductance change is only attributed to the narrow inductor strip, we have  $\alpha = L_{k0,ind}/L_0 \approx 0.54$ , where the kinetic inductance of the inductor strip  $L_{k0,ind} \approx 4.19 \text{ nH}$  and the total inductance of resonator  $L_0 \approx 7.77 \text{ nH}$ . In this case, we obtain  $I_* = 4.9 \text{ mA}$  for the standard resonator. However, the resonator is not a perfect lumped-element circuit. As shown in appendix B (see equation (B.6)), the kinetic inductance fraction can be corrected to  $\alpha' = \alpha(1 + \eta)$  if we strictly consider the current-induced kinetic inductance change from the whole resonator. Here  $\eta = \delta L_{k,frame}/\delta L_{k,ind}$  is the ratio of kinetic inductance change in IDC frame to the kinetic inductance change in inductor.  $\eta$  is usually a small factor (e.g.  $\eta \approx 3\%$  for the standard resonator) for typical lumped-element resonator designs because the current and kinetic inductance is mainly distributed in the narrow inductor strip. Therefore, it is a good approximation to only consider the kinetic inductance change of the narrow inductor strip in this work.

The inset of figure 5(d) shows the extracted  $Q_i$  and  $Q_c$  with the resonator current. We can see both  $Q_i$  and  $Q_c$  remain unchanged over a wide range of readout power. This is reasonable since  $Q_c$  is mainly determined by the coupling strength between the resonator and feed-line. The unchanged  $Q_i$  is a manifest of nonlinearity being purely reactive and not adding any dissipation. We think the absence of dielectric loss is due



**Figure 5.** (a) Measured  $|S_{21}|^2$  for the standard resonator at four different readout powers, corresponding to conditions of far below ( $a = 0.0014$ ) to well above bifurcation ( $a = 1.39$ ). The resonance frequencies are marked by the black circles. (b) Nonlinear fit of the phase-frequency curves show good agreements with experiments. (c) Measured resonance circles have same radius at selected readout powers. (d) The resonance frequency shift  $\delta f_r/f_r$  shows a good linear relationship with  $I^2$ . Note that the four red solid circles correspond to the data points at the four selected readout powers (the lowest power  $-109$  dBm corresponds to resonator current  $I \approx 2.7 \times 10^{-3}$  mA). From the slope we can derive the characteristic current  $I_*$ . The inset shows both  $Q_i$  and  $Q_c$  remain unchanged over a wide range of readout power.

to the TiN/Ti/TiN trilayer structure [36], which suppresses oxidation by protecting the Ti film and reduces the surface and interface two-level systems.

Chip1 has 7 resonators with inductor width  $w_{ind}$  varying from 1 to 30  $\mu\text{m}$ . The design of close value  $l_{ind}/w_{ind}$  makes all the resonances appear in a narrow frequency band between 1.035 GHz and 1.07 GHz. The measured transmission is shown in figure 6(a), where we can see a flat background transmission, indicating  $P_{in}$  is similar for all resonances. This helps reduce the relative error in calculating resonance current (equation (11)) for different resonators. In figure 6(b), we plot the resonance frequency shift as a function of  $I^2$  for all the resonators on Chip1. All curves show a linear relationship with  $I^2$ , thus we can extract  $I_*$  for each resonator. The derived  $I_*$  as a function of  $w_{ind}$  is plotted in figure 6(c), showing a good linear relationship between  $I_*$  and  $w_{ind}$ . Note that for the

resonator with  $w_{ind} = 10 \mu\text{m}$ , we have two identical designs but with different coupling quality factor ( $Q_c = 14.0 \times 10^3$  and  $53.2 \times 10^3$ , respectively). The derived  $I_*$  for these two resonators is very close (relative deviation  $\approx 4.7\%$ ). These all indicate that  $I_*$  is linearly related to the cross-sectional area of the inductive strip. Considering the TiN trilayer is 18 nm thick, we can derive a characteristic current density  $J_* = 27.2 \text{ mA } \mu\text{m}^{-2}$ . This suggests that we can reliably predict the nonlinear effect, in particular the maximum readout power before bifurcation occurs, once the resonator geometry and material are chosen.

Figure 6(d) shows the derived  $I_*$  for the resonators on Chip2. Chip2 has 9 resonators, which can be classified into 3 groups based on the inductor width  $w_{ind}$ . Group 1 contains Res. 1–3 with  $w_{ind} = 5 \mu\text{m}$ , Group 2 contains Res. 4–6 with  $w_{ind} = 10 \mu\text{m}$ , and Group 3 contains Res. 7–9 with  $w_{ind} =$

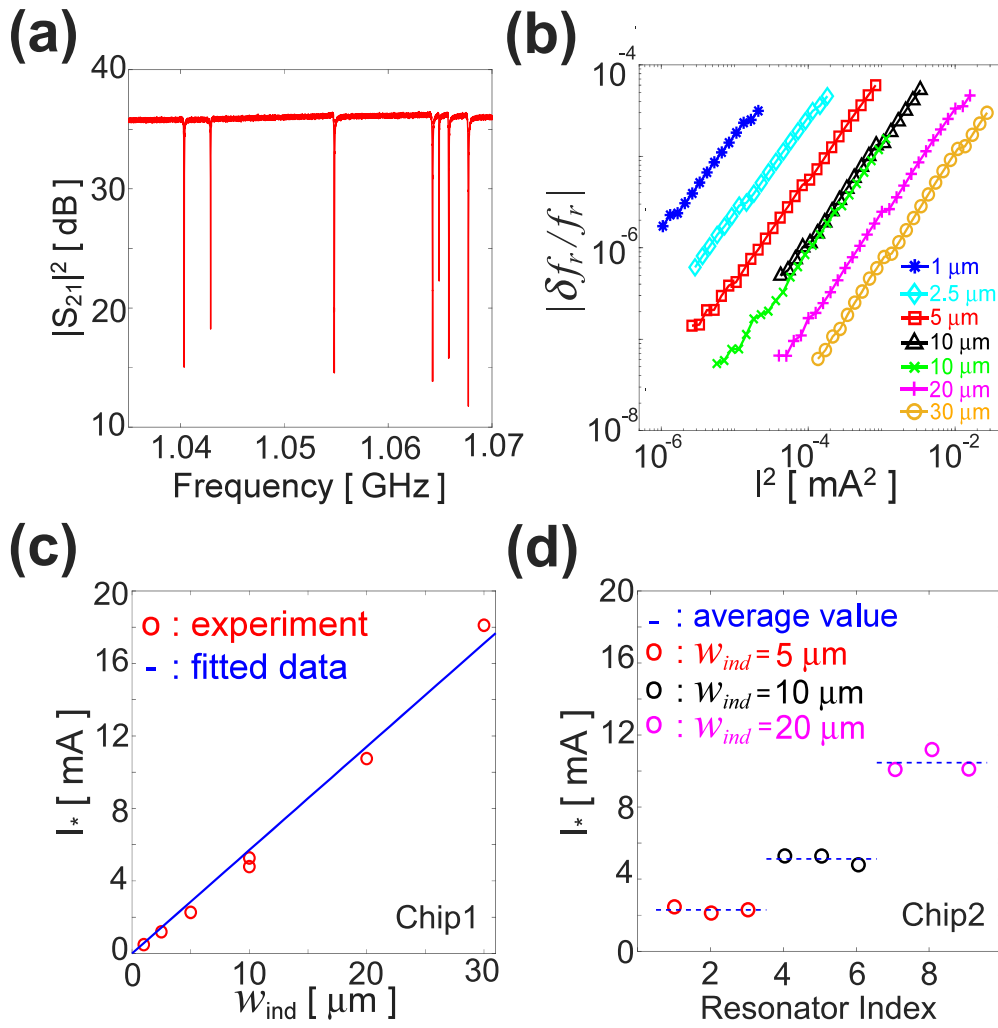


**Figure 6.** (a) Measured  $|S_{21}|^2$  for the resonators on Chip1, showing 7 resonance dips around 1 GHz. The fourth resonance (from left) corresponds to the standard resonator, which is used to draw figure 5. (b) The resonance frequency shift  $\delta f_r/f_r$  shows linear relationship with  $I^2$  for the 7 resonators with various inductor width from 1 to 30  $\mu\text{m}$ . (c) The derived characteristic current  $I_*$  is linearly related to inductor width. (d) The derived  $I_*$  for the 9 resonators on Chip2.

20  $\mu\text{m}$ . Each group includes three resonators with different inductor lengths. We can see the average  $I_*$  for each group agrees well with the results of Chip1, which further confirms that  $I_*$  for a superconducting strip is proportional to its cross-sectional area. However, the derived  $I_*$  for each group shows a certain fluctuation, which may mainly come from the uncertainty in determining  $P_{in}$  and  $I$  because the resonances are in a wider frequency band (0.6 GHz–1.5 GHz) with a fluctuating transmission background. There is also uncertainty in determining the kinetic inductance ratio  $\alpha$  for different resonators, which can also cause uncertainty in deriving  $I_*$ . Another possible reason is that the properties of superconducting film may vary from one resonator to another. Although the resonator device is made from a thin and uniform TiN/Ti/TiN trilayer film [36], which has a constant thickness (within 5%) and  $T_c$  (within 2%) across the 75 mm wafer, the proximity effect [37] among the three layers may still lead to subtle differences

in the interfaces and affect  $I_*$  uniformity. In fact, we fabricate and test two nearly identical resonators, with very close resonance frequency and coupling quality factor. The derived  $I_*$  shows little difference (within 3%), while the derived  $I_*$  for the 3 groups of resonators on Chip2 shows bigger difference  $\approx 8.6\%$ – $14.3\%$ . This indicates the material aspects might have a small contribution to  $I_*$  fluctuation, but do not play a major role.

#### 4. Conclusion

In conclusion, we present a new fitting method that can robustly and accurately fit the resonance curve in the complex  $S_{21}$  plane of a nonlinear superconducting resonator with current-dependent inductance. We demonstrate using this fitting method to successfully retrieve resonator parameters from transmission data below, near and above bifurcation. We

further use this method to retrieve  $I_*$  for lumped-element TiN resonators with various inductor designs. For each resonator, the fitted resonance frequency shift shows linear relationship with readout power, and from the slope the characteristic current  $I_*$  can be derived. We find good linear relationship between  $I_*$  and the cross-sectional area of the inductor. Our fitting method can serve as a standard fitting approach for superconducting detector, superconducting qubit and parametric amplifier data analysis where the resonator is driven in the nonlinear regime.

## Data availability statement

The data that support the findings of this study are available upon reasonable request from the authors.

## Acknowledgments

X Dai and X Liu contribute equally to this work. The TiN devices were fabricated in the NIST-Boulder microfabrication facility. This work is supported by the National Natural Science Foundation of China (Grant Nos. 61871333, 11974290), the National Science Foundation of Sichuan (Grant No. 2022NSFSC0518), the National Key Research and Development Project (No. 2016YFF0200301) and the National Institute of Metrology Fundamental Research Project (No. AKYZZ2015).

## Appendix A. Derivation of resonance current

Figure A1 shows the 2-port equivalent circuit model for the tested superconducting resonator. The input power into port 1 is  $P_{in}$ , which can be reflected at port 1 to the generator, transmitted past the resonator at port 2 to the load, and dissipated in the resonator. According to the energy conservation, we have:

$$\frac{V^2}{R} = P_{in}(1 - |S_{11}|^2 - |S_{21}|^2). \quad (\text{A.1})$$

For conditions of  $\omega C_c Z_0 \ll 1$  and close to resonance frequency  $\omega_r = 1/(LC)^{1/2}$ , the reflection  $S_{11}$  and transmission  $S_{21}$  can be easily derived:

$$S_{21} = 1 - \frac{Q/Q_c}{1 + 2jQx}, \quad S_{11} = \frac{Q/Q_c}{1 + 2jQx}, \quad (\text{A.2})$$

where  $x = (\omega - \omega_r)/\omega_r$  is the fractional frequency detuning,  $Q_c = 2C/(Z_0\omega_r C_c^2)$  is the coupling quality factor,  $Q_i = \omega_r RC$  is the internal quality factor, and  $Q$  is the total quality factor with  $1/Q = 1/Q_c + 1/Q_i$ . Then the resonator voltage and current can be derived:

$$V^2 = P_{in} \frac{2Q^2}{Q_c \omega_r C} \frac{1}{1 + 4Q^2 x^2}, \quad (\text{A.3})$$

$$I^2 = \frac{V^2}{\omega^2 L^2} \approx V^2 \omega_r^2 C^2 = P_{in} \frac{2Q^2 \omega_r C}{Q_c} \frac{1}{1 + 4Q^2 x^2}. \quad (\text{A.4})$$

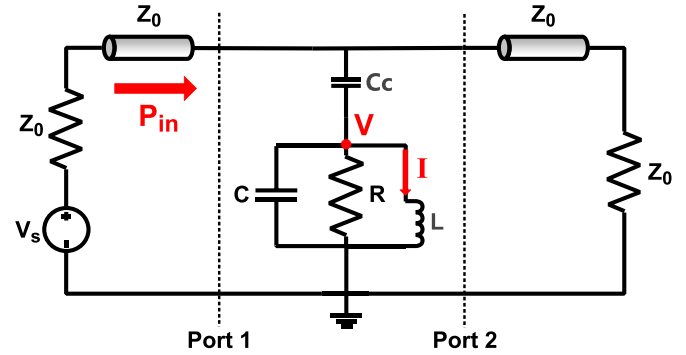


**Figure A1.** Equivalent circuit for a lumped-element resonator, which is capacitively coupled to the feed-line via a small capacitance  $C_c$ . The circuit is impedance matched everywhere, i.e. the impedance of microwave generator, transmission line and load are all  $Z_0$ .  $V$  denotes the root-mean-square (RMS) amplitude of voltage across the resonator and  $I$  denotes the RMS amplitude of current in the resonator.

On resonance,  $x = 0$ , equation (A.4) reduces to equation (11). Note that this relation holds only for impedance matching conditions.

## Appendix B. Effects of non-ideal lumped-element circuit

As shown in figure 4(a), the resonator has a lumped-element design with a narrow inductive strip which is referred as the ‘inductor’ throughout this paper. We try to derive the characteristic current  $I_*$  for this narrow inductive strip with different widths. However, the resonator is not an ideal lumped-element circuit which complicates the analysis. As shown in figure 4(b), although the current is mainly distributed in the inductor, there is a finite and position-dependent current distribution in the  $50 \mu\text{m}$  wide IDC frame which connects the IDC fingers (purely capacitive) and the inductor (purely inductive). Therefore the IDC frame also contributes to the inductance change as readout power (resonator current) changes. Then the total kinetic inductance change of the whole resonator  $\delta L$  can be divided into two parts: the kinetic inductance change in the narrow inductor strip  $\delta L_{ind}$  and in the IDC frame  $\delta L_{frame}$ . The corresponding resonance frequency shift can be written as:

$$\frac{\delta f_r}{f_{r0}} = -\frac{1}{2} \frac{\delta L}{L_0} = -\frac{1}{2} \frac{\delta L_{ind} + \delta L_{frame}}{L_0}, \quad (\text{B.1})$$

where  $L_0$  is the total inductance at low-power, which is about 7.77 nH for the standard resonator.

Supposing the amplitude of the resonance current in the inductor is  $I$ , the current dependent kinetic inductance change in the inductor is given by:

$$\delta L_{k,ind} = \frac{I^2}{I_*^2} L_{k0,ind}, \quad (\text{B.2})$$

where  $L_{k0,ind}$  is the kinetic inductance of inductor strip at low-power limit, which is about 4.19 nH for the standard resonator.



To calculate  $\delta L_{k,frame}$ , we model the IDC frame as a quasi-one-dimensional transmission line with distributive kinetic inductance  $\tilde{L}_{k0,frame}$  per unit length and position-dependent current amplitude  $I(x)$ , which approaches 0 at the position far from the inductor and reaches its maximum value  $I$  nearby the inductor. From a transmission line modal analysis, one can derive that the equivalent kinetic inductance change is weighted by the square of the current distribution:

$$\delta L_{k,frame} = \int \frac{I^2(x)}{I^2} \delta \tilde{L}_{k,frame}(x) dx, \quad (\text{B.3})$$

where  $\delta \tilde{L}_{k,frame}(x)$  is the position-dependent kinetic inductance change per unit length in the frame, which takes the form:

$$\delta \tilde{L}_{k,frame}(x) = \frac{I^2(x)}{I_{*,frame}^2} \tilde{L}_{k0,frame}, \quad (\text{B.4})$$

where  $\tilde{L}_{k0,frame}$  is the kinetic inductance per unit length of IDC frame at low-power limit. In equation (B.4),  $I_{*,frame}$  is the characteristic current for the IDC frame. We reasonably assume the characteristic current is proportional to the width of the superconducting strip so that we have  $I_{*,frame} = (w_{frame}/w_{ind})I_*$ . Then equation (B.3) can be written as:

$$\delta L_{k,frame} = \int \left( \frac{I(x)}{I} \right)^4 \left( \frac{w_{ind}}{w_{frame}} \right)^2 \frac{I^2}{I_*^2} \tilde{L}_{k0,frame} dx. \quad (\text{B.5})$$

Note that the factor of  $(I(x)/I)^4 (w_{ind}/w_{frame})^2$  in equation (B.5) is much smaller than 1 for typical lumped-element designs because  $w_{ind} \ll w_{frame}$  and the IDC frame has a smaller current distribution ( $I(x) < I$ ). We further

define  $\eta = \delta L_{k,frame}/\delta L_{k,ind}$ , then equation (B.1) can be simplified to:

$$\frac{\delta f_r}{f_{r0}} = -\frac{1}{2} \frac{I^2}{I_*^2} \frac{L_{k0,ind}}{L_0} (1 + \eta) = -\frac{1}{2} \frac{I^2}{I_*^2} \alpha (1 + \eta). \quad (\text{B.6})$$

The calculated  $\eta$  for all the resonators are shown in tables C1 and C2. We can see  $\eta$  is generally much smaller than 1, especially for resonators with narrower inductor width below 20  $\mu\text{m}$ . This indicates  $\delta L_{k,frame}$  is negligible compared to  $\delta L_{k,ind}$ , although the IDC frame contributes significant inductance to the total inductance. Therefore it is a good approximation to only consider the kinetic inductance change of the narrow inductor strip.

### Appendix C. Resonator designs and parameters

The main design parameters ( $w_{ind}$  and  $l_{ind}$ ) and measured parameters ( $f_{r0}$ ,  $Q$ , etc) for resonators on Chip1 is listed in table C1. The value of  $l_{ind}/w_{ind}$  is roughly fixed so that all resonators have resonance frequencies around 1 GHz. The resonators are all coupled to a 50 ohm feed-line and the size of the diced chip is about 5 mm  $\times$  10 mm.

The main design and measured parameters for resonators on Chip2 is listed in table C2. Chip2 has 9 resonators, which can be classified into 3 groups: Group 1 contains Res. 1–3 with  $w_{ind} = 5 \mu\text{m}$ , Group 2 contains Res. 4–6 with  $w_{ind} = 10 \mu\text{m}$ , and Group 3 contains Res. 7–9 with  $w_{ind} = 20 \mu\text{m}$ . Each group has three resonators with different  $l_{ind}$ . The measured resonance frequencies are distributed in a larger span from about 0.6 to 1.5 GHz. Note that for Res. 9 with short and wide inductive strip,  $\eta$  is not negligible.

**Table C1.** Design and measured parameters for Chip1.

Res.	$w_{ind}$ ( $\mu\text{m}$ )	$l_{ind}$ ( $\mu\text{m}$ )	$f_{r0}$ (GHz)	$Q$ ( $\times 10^3$ )	$Q_c$ ( $\times 10^3$ )	$Q_i$ ( $\times 10^3$ )	$\eta$
1	1	52	1.0249	22.8	26.2	172.8	$1.31 \times 10^{-4}$
2	2.5	140	1.0658	18.2	19.7	184.7	$8.90 \times 10^{-4}$
3	5	290	1.0677	12.7	13.4	186.0	$3.60 \times 10^{-3}$
4	10	590	1.0643	13.1	14.0	189.7	$1.48 \times 10^{-2}$
5	10	590	1.0649	42.1	53.2	185.5	$1.48 \times 10^{-2}$
6	20	1180	1.0548	15.9	17.0	187.9	$6.13 \times 10^{-2}$
7	30	1770	1.0403	18.1	20.1	177.7	0.14

**Table C2.** Design and measured parameters for Chip2.

Res.	$w_{ind}$ ( $\mu\text{m}$ )	$l_{ind}$ ( $\mu\text{m}$ )	$f_{r0}$ (GHz)	$Q$ ( $\times 10^3$ )	$Q_c$ ( $\times 10^3$ )	$Q_i$ ( $\times 10^3$ )	$\eta$
1	5	1150	0.6420	38.8	43.8	342.4	$9.40 \times 10^{-4}$
2	5	570	0.8525	21.3	21.3	259.1	$1.90 \times 10^{-3}$
3	5	290	1.0660	15.2	16.2	178.6	$3.60 \times 10^{-3}$
4	10	1160	0.8450	26.8	28.7	265.9	$7.60 \times 10^{-3}$
5	10	590	1.0621	20.1	22.1	187.0	$1.48 \times 10^{-2}$
6	10	300	1.2667	12.2	13.0	146.2	$2.84 \times 10^{-2}$
7	20	1180	1.0548	14.7	15.4	198.1	$6.14 \times 10^{-2}$
8	20	620	1.2521	17.1	18.9	146.6	0.11
9	20	320	1.4207	13.8	14.8	122.3	0.22

**ORCID iD**Y Wang  <https://orcid.org/0000-0003-2337-1181>**References**

- [1] Zmuidzinis J 2012 *Annu. Rev. Condens. Matter Phys.* **3** 169
- [2] Day P K, LeDuc H G, Mazin B A, Vayonakis A and Zmuidzinis J 2003 *Nature* **425** 817
- [3] Kreikebaum J, Dove A, Livingston W, Kim E and Siddiqi I 2016 *Supercond. Sci. Technol.* **29** 104002
- [4] Macklin C, O'Brien K, Hover D, Schwartz M E, Bolkhovskiy V, Zhang X, Oliver W D and Siddiqi I 2015 *Science* **350** 307
- [5] Doyle S, Mauskopf P, Naylon J, Porch A and Duncombe C 2008 *J. Low Temp. Phys.* **151** 530
- [6] Hubmayr J et al 2015 *Appl. Phys. Lett.* **106** 073505
- [7] Monfardini A et al 2011 *Astrophys. J. Suppl. Ser.* **194** 24
- [8] Sayers J et al 2014 *Proc. SPIE* **9153** 915304
- [9] Guo W et al 2017 *Appl. Phys. Lett.* **110** 212601
- [10] Mezzena R, Faverzani M, Ferri E, Giachero A, Margesin B, Nucciotti A, Puiu A and Vinante A 2020 *J. Low Temp. Phys.* **199** 73
- [11] Zobrist N et al 2019 *Appl. Phys. Lett.* **115** 213503
- [12] Parriani J D A, Papageorgiou A, Doyle S and Pascale E 2018 *J. Low Temp. Phys.* **193** 113
- [13] Quaranta O, Cecil T, Gades L, Mazin B and Miceli A 2013 *Supercond. Sci. Technol.* **26** 105021
- [14] Visser P, Rooij S, Murugesan V, Thoen D and Baselmans J 2021 *Phys. Rev. Appl.* **16** 034051
- [15] Thomas C, Withington S, Sun Z, Skyrme T and Goldie D 2020 *New J. Phys.* **20** 073028
- [16] Dahm T and Scalapino D J 1997 *J. Appl. Phys.* **81** 2002
- [17] de Visser P J, Withington S and Goldie D J 2010 *J. Appl. Phys.* **108** 114504
- [18] Bellenghi C, Cardani L, Casali N, Colantoni I, Cruciani A, Pettinari G and Vignati M 2020 *J. Low Temp. Phys.* **199** 639
- [19] Abdo B, Segev E, Shtempluck O and Buks E 2006 *Phys. Rev. B* **73** 134513
- [20] Gao J et al 2014 *J. Low Temp. Phys.* **176** 136
- [21] Swenson L J, Day P K, Eom B H, Leduc H G, Llombart N, McKenney C M, Noroozian O and Zmuidzinis J 2013 *J. Appl. Phys.* **113** 104501
- [22] Yurke B, Corruccini L, Kaminsky P, Rupp L, Smith A, Silver A, Simon R and Whittaker E 1989 *Phys. Rev. A* **39** 2519
- [23] White T et al 2015 *Appl. Phys. Lett.* **106** 242601
- [24] Eom B, Day P, LeDuc H G and Zmuidzinis J 2012 *Nat. Phys.* **8** 623–7
- [25] Chaudhuri S, Li D, Irwin K D, Bockstiegel C, Hubmayr J, Ullom J N, Vissers M R and Gao J 2017 *Appl. Phys. Lett.* **110** 152601
- [26] Vissers M R, Erickson R P, Ku H-S, Vale L, Wu X, Hilton G C and Pappas D P 2016 *Appl. Phys. Lett.* **108** 012601
- [27] Vissers M R, Hubmayr J, Sandberg M, Chaudhuri S, Bockstiegel C and Gao J 2015 *Appl. Phys. Lett.* **107** 062601
- [28] Bockstiegel C, Wang Y, Vissers M R, Wei L F, Chaudhuri S, Hubmayr J and Gao J 2016 *Appl. Phys. Lett.* **108** 222604
- [29] Guan H, Dai M, He Q, Hu J, Ouyang P, Wang Y, Wei L F and Gao J 2020 *Supercond. Sci. Technol.* **33** 075004
- [30] Khalil M S, Stoutimore M J A, Wellstood F C and Osborn K D 2012 *J. Appl. Phys.* **111** 054010
- [31] Petersan P J and Anlage S M 1998 *J. Appl. Phys.* **84** 3392
- [32] Gao J 2008 *PhD Thesis* Caltech
- [33] Probst S, Song F B, Bushev P A, Ustinov A V and Weides M 2015 *Rev. Sci. Instrum.* **86** 024706
- [34] Annunziata A J, Santavica D F, Frunzio L, Catelani G, Rooks M J, Frydman A and Prober D E 2010 *Nanotechnology* **21** 445202
- [35] Kubo T 2020 *Phys. Rev. Res.* **2** 033203
- [36] Vissers M R, Gao J, Sandberg M, Duff S M, Wisbey D S, Irwin K D and Pappas D P 2013 *Appl. Phys. Lett.* **102** 232603
- [37] Gurevich A and Kubo T 2017 *Phys. Rev. B* **96** 184515